Co-hydrothermal carbonization of swine and chicken manure: Influence of cross-interaction on hydrochar and liquid characteristics

Published in: *Science of the Total Environment*

Citation for published version: Li, Q., Zhang, S., Gholizadeh, M., Hu, X., Yuan, X., Sarkar, B., Vithanage, M., Mašek, O., Ok, Y. S. (2021) Co-hydrothermal carbonization of swine and chicken manure: Influence of cross-interaction on hydrochar and liquid characteristics. *Science of the Total Environment*. 786: 147381. doi: 10.1016/j.scitotenv.2021.147381.

Document version: Accepted peer-reviewed version.

Co-hydrothermal carbonization of swine and chicken manure: Influence of cross-interaction on hydrochar and liquid characteristics

Qingyin Li[a], Shu Zhang[b], Mortaza Gholizadeh[c], Xun Hu[a,*], Xiangzhou Yuan[d,e **], Binoy Sarkar[f], Meththika Vithanage[g], Ondřej Mašek[h], Yong Sik Ok[e, ***]

[a] School of Materials Science and Engineering, University of Jinan, Jinan 250022, Shandong, China

[b] College of Material Science and Engineering, Nanjing Forestry University, Nanjing 210037, Jiangsu, China

[c] Faculty of Chemical and Petroleum Engineering, University of Tabriz, Tabriz, Iran

[d] Department of Chemical & Biological Engineering, Korea University, 145 Anam-ro, Seongbuk-gu, Seoul 02841, Republic of Korea

[e] Korea Biochar Research Center, APRU Sustainable Waste Management Program & Division of Environmental Science and Ecological Engineering, Korea University, Seoul 02841, Republic of Korea

[f] Lancaster Environment Centre, Lancaster University, Lancaster, LA1 4YQ, United Kingdom

[g] Ecosphere Resilience Research Center, Faculty of Applied Sciences, University of Sri Jayewardenepura, Nugegoda 10250, Sri Lanka

[h] UK Biochar Research Centre, School of Geosciences, University of Edinburgh Alexander Crum Brown Road, Crew Building-EH9 3JN, Edinburgh, UK

* Corresponding author: +86-531-8973-6201, E-mail: Xun.Hu@outlook.com

** Corresponding author: +82-2-3290-3926, E-mail address: yuan0125@korea.ac.kr

*** Corresponding author: +82-2-3290-3044, E-mail: yongsikok@korea.ac.kr

Graphical Abstract

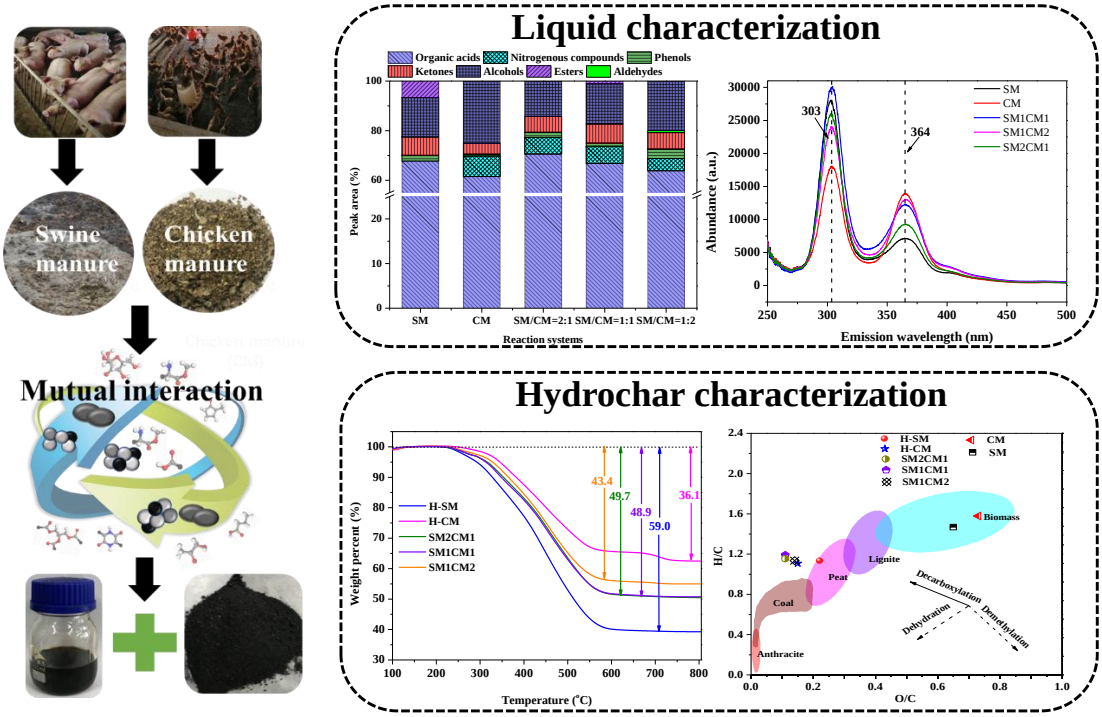

Highlights

- Co-HTC of manure mixture enhanced the hydrochar yield compared to individual HTC.
- The interaction of HTC intermediates from the mixed manures improved deoxygenation.
- Co-HTC favored carbon and nitrogen enrichment in the hydrochar.
- Synergistic effect of co-HTC improved the combustion properties of hydrochar.
- Interaction of co-HTC intermediates impacted the features of liquid products.

Abstract

Swine and chicken manures are abundant solid wastes that can be converted into carbonaceous materials through hydrothermal carbonization (HTC). Owing to their unique biochemical compositions, co-HTC of these two types of manures may have significant implications for the generated products. We investigated the co-HTC of swine manure and chicken manure to understand the influence of the interaction between contrasting manures on the properties of the derived products. The results indicated that co-HTC treatment enhanced the formation of solid product and improved the C and N contents, heating value, and energy yield of the resulting hydrochar. Regarding the ignition temperature and comprehensive combustion index, the combustion properties of the hydrochar were enhanced owing to the mutual effect of the HTC intermediates. Additionally, the interaction of the intermediates significantly impacted the transfer of nitrogenous species and generation of organic acids and organic polymers with fused-ring structures. Therefore, co-HTC processing of animal manures could potentially provide a sustainable pathway for the conversion of animal waste into solid products with improved characteristics compared to those produced by treating the two feedstocks separately.

Keywords: Biowaste; Hydrochar; Animal waste; Clean energy; Circular economy

1. Introduction

Animal husbandry has rapidly expanded in recent years, generating large quantities of manures that pose an environmental threat (Hu et al., 2017; Yuan et al., 2018). Manure composting is a primary upcycling technique to deal with large amounts of animal waste. However, manure composting inevitably leads to bad odor and soil pollution because of the accumulation of organic pollutants, such as the veterinary antibiotics contained in manure (Lang et al., 2019a). Furthermore, the bioavailability and toxicity of heavy metals increases during composting (Guo et al., 2012; He et al., 2009). Thus, identifying a sustainable pathway for the safe and effective management of different animal manures is significant, in line with the concept of a circular economy. Animal manures hold a great potential as feedstocks for the generation of heat and power and the production of materials and chemicals owing to their high organic content.

Hydrothermal carbonization (HTC) has been widely adopted to treat wet feedstocks such as animal manure to produce solid fuels. This is because the HTC process generally operates at a moderate temperature and in an aqueous environment, facilitating the direct utilization of wet feedstock without the need for pre-drying (Sharma et al., 2020; Wang et al., 2018a). Additionally, HTC treatment promotes a reduction in the bioavailable fractions of heavy metals whereas the stable fraction of heavy metals is increased possibly through complexation, precipitation, adsorption, or other pathways during the reaction process, suggesting that HTC facilitates the immobilization of heavy metals to minimize their environmental impact (Wang et al., 2019). The structure of the resulting hydrochar is similar to that of coal, thus making it applicable as a solid fuel, soil amendment, and adsorbent (Nogueira et al., 2019; Tan et al., 2016). Previous studies on the HTC of swine manure or chicken manure have demonstrated their potential in the production of solid fuels (Lang et al., 2019b; Mau et al., 2016).

Several reactions occur during HTC, including hydrolysis, decomposition, re-polymerization, and condensation (Funke & Ziegler, 2010). The reaction mechanisms

of the feedstock components and the derived intermediates determine their reaction networks. Various feedstocks generate intermediates that exhibit different charring potentials (Heidari et al., 2019; Lu & Berge, 2014). Thus, it is feasible to preferentially modifying the charring process to generate more solid products with desirable properties by altering the types or abundance of the derived intermediates. Swine manure and chicken manure exhibit distinct properties and compositions, thus generating different reaction intermediates. The underlying interactions among the degraded fragments may impact the characteristics of HTC-derived products. Understanding this mutual interaction process facilitates the evaluation of the HTC mechanism in animal manure. Moreover, the practical relevance of the co-HTC of various animal manures is the reduction in the industrial operation cost, as the segregation of animal waste based on origin is not required.

In this study, we investigated the co-HTC mechanism of two types of animal wastes including swine manure and chicken manure, and analyzed the produced liquid and hydrochar using various techniques. The primary purpose of this work were to: (1) evaluate the physicochemical properties of hydrochar produced by co-HTC at different mixing ratios (compositions, surface functional groups and combustion characteristics); (2) investigate the feature of the chemical components of co-HTC liquid; and (3) explicit the mutual interaction effect during co-HTC.

2. Materials and methods

2.1. Materials

Swine manure (SM) and chicken manure (CM) were acquired from a pig and poultry farm in Jinan, China. The raw materials were dried in an oven, followed by grinding in a ball-mill equipment and sieving to obtain the required particle size fraction (20–40 mesh). All the chemicals used (analytical grade) in the study were supplied from Tianjin Fuyu Fine Chemical Co., Ltd. (Tianjin, China).

The biochemical compositions of SM and CM were investigated to evaluate their co-HTC behavior, which was determined based on the dried manure feedstock. The

protein content was determined using Kjeldahl method (National Standard in China GB 5009.5-2010). Lipid content was measured with Soxhlet extraction method (National Standard in China GB 5009.6-2016). The carbohydrate content was calculated via mass difference (carbohydrates% = 100% - lipids% - proteins% - ash%, dry basis) (Chen et al., 2017). The lipid and carbohydrate contents of SM were 9.6% and 54.7%, respectively, which were higher than those of CM (6.3% and 44.9%). However, the protein content of SM (12.5%) was lower than that of CM (16.7%). These differences in biochemical composition could affect their mutual interaction during the co-HTC process.

Additionally, the inorganic elements in SM and CM (dry basis) were detected using 3600 X-ray fluorescence (XRF, Thermo Fisher Scientific Company, Waltham, MA). The content of inorganic species was calculated based on manure ash. The results showed that Ca, Si, and K were the primary inorganic species in SM (30.86%, 16.83%, and 10.48%, respectively) and CM (21.92%, 27.16%, and 12.19%, respectively). In addition, traces of Mg, Al, Na, and Fe species were also detected in the raw materials.

2.2. Hydrothermal carbonization

The HTC experiments were conducted at 240 ℃ for 10 h in a 100-mL stainless autoclave. In a typical run, a mixture of 5 g of feedstock (SM, CM, or their mixture with mass ratios of 2:1, 1:1, or 1:2, respectively) and 50 mL of deionized water was placed within the equipment. The reactor was assembled and purged with nitrogen to displace the air inside and subsequently pressurized up to 3 MPa using nitrogen before heating. The reactor was maintained at a pre-set temperature for the required duration before being allowed to cool naturally. The solid product was separated from the solid-liquid mixture via vacuum filtration. The corresponding filtrate was collected for further analyses. The solid fraction was dried in an oven at 105 ℃ for 12 h. The solid yield was determined by weighing the mass of the dried solid product.

$$Hydrochar\ yield = \frac{Weight\ of\ hydrochar}{Weight\ of\ raw\ feedstocks} \times 100\% \quad (1)$$

For simplicity, the hydrochars derived from SM, CM, and their mixture are

indicated as H-SM, H-CM, SM2CM1, SM1CM1, and SM1CM2, respectively, where H represents the hydrothermal carbonization, and the numbers represent the mass ratio of SM to CM in the mixture. All solid samples were milled to a fine powder for characterization.

2.3. Characterization methods

2.3.1. Analysis of hydrochar

The contents of C, H, N, and S in the hydrochar were examined by a Thermo Scientific Flash 2000 Organic Elemental Analyzer (CHNS Analyzer). The O content was obtained by subtracting the contents of C, H, N, S, and ash. Proximate analysis of the hydrochar was conducted based on the Chinese national standard procedures (GB/T 212-2008). Important indicators, including the higher heating value (HHV), C and N recovery rates, and energy yield derived from the solid samples, were calculated using the following equations (Channiwala & Parikh, 2002; Kim et al., 2016):

$$HHV = 0.3491\ C\% + 1.1783\ H\% + 0.1005\ S\% - 0.1034\ O\% - 0.015\ N\% - 0.021\ ash\% \quad (2)$$

$$\text{C recovery rate} = \text{Hydrochar yield} \times \frac{C_{in\ hydrochar}}{C_{in\ feedstock}} \quad (3)$$

$$\text{N recovery rate} = \text{Hydrochar yield} \times \frac{N_{in\ hydrochar}}{N_{in\ feedstock}} \quad (4)$$

$$\text{Energy yield} = \text{Hydrochar yield} \times \frac{HHV_{hydrochar}}{HHV_{feedstock}} \quad (5)$$

The surface functional groups of the HTC solids and feedstocks were obtained using Fourier-transform infrared spectroscopy (FTIR; Nicolet iS50). The sample was mixed with KBr at a ratio of 1: 199 and compacted into a pellet. The background from the air scans was subtracted from these samples. FTIR spectra in the 400–4000 cm^{-1} region were observed after 16 scans. Additionally, in situ diffuse reflection infrared Fourier-transform spectroscopy (DRIFTS) analysis was conducted to investigate the thermal stability of the functional groups in the solid. The temperature of the solid increased to 700 °C at a heating rate of 10 °C/min. During heating, changes in the functional groups were recorded. The crystal structures of the hydrochars were identified with X-ray

diffraction (XRD, Rigaku Ultima IV) with a Cu Kα radiation source. These samples were tested from 10° to 80° with a scan rate of 20 °/min.

To evaluate the combustion properties of these solid samples, a thermogravimetric analyzer (TGA) was employed to obtain the corresponding thermogravimetric (TG) and differential thermal gravimetric (DTG) profiles. The solid samples (around 10 mg) were heated to 900 ℃ at a heating rate of 20 ℃/min. A comprehensive combustion index S was used to assess the combustion property of the hydrochar, which is defined as follows (Chen et al., 2018):

$$S = \frac{DTG_{max} \times DTG_{mean}}{Ti^2 \times Tf} \tag{6}$$

where DTG_{max} and DTG_{mean} represent the maximum mass loss rate and average mass loss rate, respectively. T_i stands for the ignition temperature at which the solid fuel starts burning, and T_f represents the burnout temperature at which the combustion reaction ends.

The simplified first-order kinetic model was used with the Coats-Redfern integral method to calculate the activation energy for combustion (Zheng et al., 2019). The adopted equations are as follows:

$$\alpha = \frac{m_0 - m_t}{m_0 - m_\infty} \tag{7}$$

$$\ln\left[\frac{-\ln(1-\alpha)}{T^2}\right] = \ln\frac{AR}{\beta E} - \frac{E}{RT} \tag{8}$$

where α is the conversion rate; m_0, m_t and m_∞ refer to the initial mass, mass at a certain time t, and final mass of solids, respectively; β is the heating rate; T is the reaction temperature; R means the universal gas constant; and A and E represent the pre-exponential factor and activation energy, respectively.

Additionally, the corresponding theoretical value was calculated based on the parameters from the single feedstock and mixing ratio. A synergistic coefficient (SC) was introduced to describe the difference between the experimental values and the theoretically calculated values. The SC could quantitatively evaluate the extent of synergistic effects from the co-HTC of SM and CM, and was calculated as follows:

$$\mathrm{SC} = \frac{Experimental\ value - Theoretical\ value}{Theoretical\ value} \times 100\% \tag{9}$$

2.3.2. Characterization of liquid products

The chemical components in the liquid products were analyzed using gas chromatography-mass spectrometry (GC-MS Shimadzu, QP2020). A capillary column, 30 m length and 0.25 mm diameter, was utilized for the separation of organics. The column temperature increased from 50 to 250 ℃ at a heating rate of 10 ℃/min and maintained for 10 min. The carrier gas used was helium with a flow rate of 4.0 mL/min. The specific compositions of organics in the liquid were identified using the standard library (NIST MS Search 2014), and the relative content of each species was determined using the area normalization method.

An RF-6000 UV-fluorescence spectrophotometer (Shimadzu, Japan) was employed to analyze the structural characteristics of the soluble polymeric components in the liquid. The samples were diluted with ethanol to 800 ppm before examination. The initial excitation wavelength and emission wavelength were set to 220 and 250 nm, respectively. With a scan speed of 600 nm/min, the fluorescence spectra were acquired in the synchronous mode. In the case of 3D fluorescence spectra, the excitation wavelengths were ranged from 200 to 400 nm, and the emission wavelengths from 250 to 500 nm were selected for the sample analysis. The slit widths of the excitation and emission were 5.0 nm at a scan speed of 600 nm/min.

3. Results and discussion

3.1. Hydrochar yield from different HTC systems

The yield of solid products from the HTC of individual SM, CM, and their combinations were investigated. Each experiment was conducted in triplicate, and the average values and standard deviations are displayed in Fig. 1. The solid yield (44.57%) of the CM feedstock was higher than that from the SM feedstock (43.41%), which was attributed to their different biochemical compositions. Notably, a higher yield of hydrochar was derived from the manure mixtures (50.17% from SM2CM1, 52.57% from SM1CM1, and 54.57% from SM1CM2). Additionally, the comparison of

hydrochar yields between the experimental and theoretical values indicated that blending of the feedstocks had a remarkable effect on the formation of the solid products during the co-HTC process, as evident from the considerably higher solid yields. Furthermore, the difference between the experimental and calculated yields was expressed through the SC defined in Eq. 7. The SC increased with increasing proportions of CM, implying that the addition of CM favored the formation of hydrochar. Due to high protein content of CM, the increased proportion of CM in the mixture may enhance the interactions among intermediates from the degraded protein and carbohydrate fractions in the mixed manures, and consequently improve the solid yield (Li et al., 2019b).

3.2. Basic properties of the feedstock and hydrochar

The ultimate analysis, atomic ratios, and recovery rates of the raw feedstocks and hydrochars are presented in Table 1. The C content of the hydrochars was higher than that of the feedstocks, except for H-CM. This phenomenon was mainly due to the hydrolysis and carbonization occurring during HTC, which affected the C content. The H and O contents of the hydrochars decreased considerably, which was possibly attributed to the degradation of organic species in the feedstock. The molar ratios of H/C and O/C in the feedstock and hydrochar are shown in the Van Krevelen diagram (Fig. 2). After the HTC treatment, an evident reduction in the H/C and O/C ratios of the hydrochars occurred due to dehydration and decarboxylation reactions (Cantero-Tubilla et al., 2018). Both the H/C and O/C ratios derived from H-CM (1.20 and 0.15, respectively) were lower than those of H-SM (1.23 and 0.22, respectively), suggesting that organic matter readily degraded in the CM. The O/C ratio of the co-HTC solids exhibited a pronounced decline in comparison with that of the individual feedstock. This implied that the co-presence of SM and CM improved the deoxygenation performance, which helped to increase in the heating value of the resulting hydrochar. Besides, the H/C ratios decreased with increasing proportions of SM, which was possibly associated with the enhanced dehydration due to the mutual interaction of

reactive biochemical fragments. Consequently, the C content of the hydrochars increased owning to co-HTC treatment.

The recovery of carbon and nitrogen from the tested samples is also presented in Table 1. Compared with H-CM and H-SM, a higher C recovery rate was obtained from the co-HTC solids, indicating that the co-HTC process favored the enrichment of carbonaceous species in the hydrochars. This was likely due to the re-polymerization and carbonization reactions among the reactive substances produced during the thermo-degradation of SM and CM biomolecules (Cao et al., 2011). The lowest N recovery rate was found for H-CM, implying that a substantial amount of N was transformed into the liquid and gas phases instead of the solid phase. However, co-treatment of SM and CM was beneficial for the enrichment of nitrogenous species in the hydrochars during the co-HTC process. The preservation of N in the char is particularly important if it is aimed to be used as a fertilizer or for other applications where N-doped carbons exhibit superior performance, such as environmental remediation (Kang et al., 2018).

The proximate analysis, HHV, and energy yield of the solid samples are displayed in Table 2. The enhancement of the fixed carbon content in the hydrochars was also indicative of a high degree of carbonization (Kim et al., 2014). The decrease in the volatile matter content due to its degradation at high temperatures was responsible for the decreased H, N, and O contents of the hydrochars. As expected, the ash content of the hydrochars was higher than that of the feedstocks, which may be ascribed to the transformation of volatile matter or other components. The hydrochar generated during the HTC of the mixed feedstock showed higher C and H contents, thus resulting in a higher heating value compared to that of H-CM. Moreover, increasing the ratio of SM during co-HTC increased the heating value. These results indicated that mixing of SM with CM could enhance the fuel properties of hydrochars. Additionally, the co-HTC of SM and CM also improved the energy yield of the hydrochars compared to those from the individual feedstocks.

Additionally, the synergistic coefficient was utilized to reveal the mutual effect between the SM and CM. The co-presence of SM and CM exerted a synergistic

interaction during the co-HTC process (Table 3). The combination of feedstocks at various mixing ratios showed a prominent influence on the hydrochar properties. The highest synergistic coefficient related to the C content, C recovery rate, and energy yield were achieved from SM1CM1, whereas the highest value of fixed carbon was obtained from SM2CM1. The synergistic effects from the mixture could possibly be ascribed to two reasons. Firstly, a Maillard reaction may have occurred among the intermediates derived from the degradation of the protein and carbohydrate fractions of the feedstocks (Wei et al., 2018). Alternatively, the presence of inorganic species in the feedstocks could have affected the decomposition of the fragments and further impacted the formation of solid products (Liu et al., 2019).

3.3. Thermal characteristics and combustion behavior of the hydrochars

The combustion performance of the feedstocks and derived hydrochars was investigated via thermogravimetric characterization in air. Figures. 3a-c illustrate the TG and DTG profiles of the feedstocks and hydrochars obtained from the different mixed systems; Fig. 3d shows the mass loss percentages of all the solid samples. According to the TG analysis of raw materials, the total mass loss from SM (82.4%) was higher than that from CM (66.6%), implying that a larger quantity of volatile organics was present in the SM than in CM. The corresponding temperatures of the mass loss peaks for SM were lower than those for CM. Additionally, the mass loss from the SM-derived solid was higher than that from the CM-derived solid. In the case of mixture systems, the mass loss from SM1CM2 was remarkably lower than that from the other combinations, which could be associated with the higher ash content in CM.

The raw materials, H-SM, and H-CM exhibited two mass loss peaks, whereas the mixed feedstocks exhibited three characteristic peaks. The first peak (at approximately 288 °C) in the DTG profile of the feedstocks was probably associated with the degradation of volatile matter containing protein and carbohydrate fractions (Fig. 3a) (Xu et al., 2018). The second peak located at around 460 and 500 °C for SM and CM was ascribed to the transformation of fixed carbon (Xu et al., 2019a). The initial

decomposition temperature of the resulting hydrochars significantly increased, owing to the partial decomposition of organics during the HTC treatment. Notably, a wide peak between 210 and 613 °C in the DTG graph of H-CM suggested that the degradation rate of the organic species was slower than that of the feedstocks, possibly because of the highly stable organics in the hydrochar. Considering the DTG profiles of the feedstock mixtures, a fresh peak at around 255 °C indicated the presence of light volatile matter, which could be the new organic species derived from the interaction of the HTC intermediates. This result further verified that the intermediates produced from the feedstocks underwent carbonization during their mutual interaction. The second and third peaks at around 330 and 450 °C represented the decomposition of heavy volatile matter and fixed carbon, respectively. All the peak temperatures for the co-HTC hydrochars were similar, whereas the rates of mass loss varied remarkably. In the case of SM2CM1, the mass loss rate for the peaks was higher than that for the other combinations. This implied that increasing the proportion of SM in the mixture would introduce more volatile matter, consequently increasing the DTG_1 and DTG_2 peaks. Moreover, the occurrence of cross-linking reactions among the carbohydrate-derived sugar species and protein-derived amino acids would further convert the organic species into fixed carbon via polymerization and aromatization reactions (Wang et al., 2018b). Thus, the DTG_3 peak was high for the hydrochar obtained from the co-HTC of SM2CM1.

Furthermore, some key combustion process characteristics were measured to evaluate the combustion performance of the co-HTC solids, as displayed in Table 4. The ignition temperatures (T_i) of the co-HTC solids were lower than those of H-SM and H-CM, implying that co-HTC treatment improved the combustion properties of the products. However, the burnout temperature (T_f) of the co-HTC solids was lower than that of the H-CM. The thermal degradation behavior of these samples was also evaluated using the comprehensive combustion index S. A higher S value of hydrochar suggested that the products were easier to ignite (Xu et al., 2019b). The S values of SM2CM1 and SM1CM1 were higher than those of H-SM and H-CM, implying that co-

HTC of the feedstock mixtures could improve the combustion properties of the hydrochar owning to the mutual biochemical interaction of the derived intermediates, as previously discussed.

To further evaluate the combustion behavior of the feedstocks and derived hydrochars, the kinetic parameters were determined from the DTG results. Based on previous studies, a first-order reaction model was employed to investigate the combustion performance (Luo et al., 2011). The thermal decomposition of the solid samples was divided into three stages, and the corresponding temperature ranges, activation energy, and correlation coefficients are presented in Table 5. A high correlation coefficient (R^2 > 0.93) implied that the first-order kinetic model appropriately expressed the combustion process. The combustion process of raw materials exhibited two reaction stages. In the first stage, the activation energy of SM was lower than that of CM, indicating that SM was easier to burn. This phenomenon was in good agreement with the low ignition temperature of SM. In the second combustion stage, the E value obtained from SM was higher than that from CM, indicating a higher stability of the fixed carbon in SM. Nevertheless, the E value in H-CM was higher than that in H-SM. This phenomenon was possibly attributed to the reactions including hydrolysis and carbonization of the manure components that may affect its combustion properties after HTC treatment (Li et al., 2019a).

In stage 1, the E value obtained from SM2CM1 was the highest among the mixed feedstock systems (Table 5). In stage 2, the E values of the co-HTC solids were obviously higher than those of the single feedstock products. This implied that the volatile species in the co-HTC hydrochars were more stable, possibly because of the mutual cross-linking reaction of the degraded biomolecule fragments. In stage 3, the E value of the co-HTC solids was lower than that of H-CM, demonstrating that the co-HTC of CM with SM improved the combustibility of the fixed carbon in the hydrochar.

3.4. Surface functional groups of the hydrochars

The functional groups on the surface of the solid samples and raw materials were

determined by FTIR characterization, as shown in Fig. 4a. Co-HTC of SM and CM had no remarkable effect on the distribution of the functional groups on the hydrochars. The absorption bands at around 3410 cm^{-1} represented the vibration of the hydroxyl group (Zhang et al., 2015). In comparison to SM and CM, the intensity of the -OH band was weaker for the hydrochars, being attributed to the dehydration occurring during the HTC. The peaks from 2950 to 2850 cm^{-1} were related to the antisymmetric and symmetric stretching vibration of the alkyl groups (Parshetti et al., 2013). The relative intensities of the alkyl bands became stronger after the HTC treatment, indicating an increased hydrocarbon content in the hydrochars. The bands at around 1650 cm^{-1} in the feedstock spectra showed the presence of -C=N in amide groups (de Oliveira Silva et al., 2012), which completely disappeared in the hydrochars. This phenomenon revealed the degradation of the protein and lipid fractions in the raw materials, and some N-containing components were transferred into the liquid phase.

Due to the overlap of bands from 1800 to 1500 cm^{-1}, all hydrochar spectra were deconvoluted into three specific peaks (Figs. 4b-f). The first fitted peak, centered at around 1700 cm^{-1}, belonged to the -C=O groups of aliphatic carboxylic acids, which mainly originated from the dehydration of the carbohydrate fraction (Lievens et al., 2011). The second band at ca. 1620 cm^{-1} was related to the stretching vibration of carbonyl groups from the hydroxyl unsaturated aldehydes/ketones (Lievens et al., 2011). The third peak at ca. 1570 cm^{-1} combined with the absorption at 1450 cm^{-1} were attributed to the characteristics of aromatic rings (Zhai et al., 2013), and their intensities in the hydrochar spectra were stronger than those of the raw materials. The FTIR results corroborated the fact that the carbonization reaction promoted the formation of aromatic structures during HTC. Additionally, the intensity of the peak at 1020 cm^{-1} associated with the -C-O-C vibration mode was enhanced in the hydrochars when compared with the feedstock spectra, implying that the aliphatic ether bonds were difficult to degrade (Peng et al., 2016). Bands in this region could also occur because of the -Si-O group in the ash of the hydrochars (Lang et al., 2018).

The surface chemical characteristics of the co-HTC hydrochars, which are affected

by the increasing treatment temperature, were further explored. The evolution of functional groups during the thermal treatment was investigated using DRIFTS analysis under a N_2 atmosphere (Fig. 5). Additionally, the DRIFTS results of the hydrochars derived from the individual feedstocks are displayed in Fig. S1 in the Supplementary Material. In the entire sample spectra, the intensity the -OH peak (at ca. 3300 cm^{-1}) declined with increasing temperature, implying that the hydroxyl groups were eliminated through dehydration at elevated temperatures. At higher temperatures, the band at about 3010 cm^{-1} revealed the presence of =C-H groups in alkenes, which possibly originated from the dehydration and cracking of the alkane components (Zhou et al., 2020). The absorption in the spectral range of 2900-2800 cm^{-1} belonged to the vibration of C-H groups in alkanes. Moreover, the band intensity increased dramatically with increasing temperature, which was consistent with the enhanced C-H bending vibration at ca. 970 cm^{-1} (Apaydın-Varol & Pütün, 2012). Such phenomenon implied that the abundance of the hydrocarbon species was enhanced after the HTC treatment, resulting in an improved degree of carbonization of the solid samples. Besides, the intensity of the peak related to carbonyl groups (at ca. 1730 cm^{-1}) initially increased, possibly due to dehydration and the Maillard reaction occurring between the carbohydrate- and protein-derived intermediates. Subsequently, the peak intensity at 1730 cm^{-1} decreased at higher temperatures, likely because of decarbonylation. Notably, the C=N band at about 1660 cm^{-1} became stronger during the thermal treatment, indicating the formation of N-containing species on the surface of the solid samples. The enhancement of the band intensity attributed to the C=C groups (at around 1600 and 1450 cm^{-1}) along with the increasing temperature indicated an improvement in carbonization. In comparison with the hydrochar of the individual feedstock, changes in the evolution of the C=C and C=N groups in the co-HTC hydrochar spectra suggested an enhancement in the carbonization degree and generation of nitrogenous species, which further affected the formation of the hydrochar and its properties.

3.5. Inorganic components of the hydrochars

The crystalline structures of the inorganic species in the raw materials and hydrochars were determined by XRD characterization, and the results are shown in Fig. S2 in the Supplementary Material. Three types of inorganic crystalline phases were detected in the solid samples. The diffraction reflections at 2θ = 21° and 26° were indicative of quartz in SM and CM, and those at 2θ = 29°, 36°, and 39° confirmed the presence of calcite (Cao & Harris, 2010; Xin et al., 2018). The reflections at 2θ = 28° and 35° were likely associated with calcium phosphate (Lang et al., 2019b). The corresponding reflection intensity in the XRD patterns of CM and H-CM was higher than that of SM and its derived hydrochar, which was attributed to the possible sintering of the existing inorganic species. The crystallite sizes of the minerals were calculated, and the results are listed in Table S1. The crystallite sizes of $CaCO_3$ and SiO_2 in the co-HTC hydrochars were larger than those in H-SM, whereas the crystallite sizes of $Ca_2P_2O_7$ became smaller. This phenomenon proved that the mutual interaction of chemical species also affected the evolution of inorganic components in the hydrochars.

3.6. Chemical composition and conjugated degree of liquid

The chemical composition of the liquid derived from the HTC system was analyzed using GC-MS (Table S2). According to their structural characteristics, the liquid components were classified into seven groups: organic acids, nitrogenous compounds, phenols, ketones, alcohols, esters, and aldehydes. The liquid from the co-HTC system contained higher amounts of organic acids than those from the individual feedstock (Fig. 6). The increased fraction of organic acids in the co-HTC liquids could be attributed to the enhanced cracking of carbohydrates such as cellulose and xylan (Deng et al., 2014). In addition, the hydrolysis of lipids and deamination of proteins could also produce acidic species (Li et al., 2014; Wilson & Novak, 2009). Nitrogen-containing species were mainly produced during the protein degradation. Additionally, the ammonium produced from the deamination of proteins would react with carbohydrate-derived intermediates to form nitrogenous substances (Xu et al., 2020).

The relative abundance of N-containing components was lower in the co-HTC liquids than in the CM, which was possibly ascribed to further transformations such as thermal degradation and condensation. The phenolic components primarily originated from the decomposition of lignin and the condensation of cellulose-derived species (Singh et al., 2014; Tymchyshyn & Xu, 2010). The combined feedstock systems showed no noticeable effect on the formation of phenolic species, as their relative amounts varied slightly. The relative contents of alcohols and esters decreased after the co-HTC process, likely because they were converted into other organic compounds. However, N-containing heterocyclic components generated from the interaction of the protein and carbohydrate fractions were not detected in the liquid phase, as they were presumably further polymerized into the solid phase.

To gain insight into the abundance of π-conjugated structures in the liquid products of the HTC process, the liquids were characterized by UV-fluorescence spectroscopy. Based on the previous study (Mourant et al., 2013), the absorption at around 300 nm represented the presence of chemical species with two fused aromatic rings, and the peaks at about 360 nm referred to the chemical compounds with more than three fused benzene rings. Compared with the liquid from the HTC of CM, the peak intensity of the SM-derived liquid at 303 nm was higher, whereas that at 364 nm was lower (Fig. 7a). During the HTC process, the organic substances present in SM and CM were decomposed into reaction intermediates, which further polymerized to form aromatic structures. According to this hypothesis, a number of polymers with larger π-conjugated ring systems were formed in the CM-derived liquid, whereas major organics with smaller π-conjugated structures were produced from the HTC of SM. In the mixed feedstocks, various mixing ratios had different impacts on the formed polymers. In the case of SM1CM1, the intensity of the peak at 303 nm was higher than that of the other mixture systems, whereas for the SM1CM2 system, a higher peak intensity was achieved at 364 nm.

Based on the peak intensity of the liquid from the individual feedstocks and their mixtures, the calculated intensity was compared with the experimental data (Fig. 7b).

The experimental values of the combined feedstock systems were higher than the theoretical values, except for the peak at 364 nm from SM2CM1. These phenomena indicated that the mutual interaction of the fragments generated from CM and SM could promote the formation of unsaturated species. A large difference was observed between the experimental and calculated intensities at 303 nm for SM1CM1, suggesting a stronger interaction between the blending feedstocks.

To further study the characteristics of the liquid components from the different reaction systems, 3D fluorescence spectra were employed (Fig. 8). According to previous work, the spectra can be divided into five regions representing varied types of fluorescent substances (Chen et al., 2003). The observed regions I and II at the shorter excitation and emission wavelengths correspond to chemical species similar to simple aromatic proteins, and region III is associated with fulvic acid-like materials. Region IV at moderate excitation wavelengths and shorter emission wavelengths indicates the existence of soluble microbial byproduct-like substances or other large aromatic proteins. Additionally, region V is related to humic acid-like compounds. In comparison with the CM-derived liquid, the intensity of region IV from the mixed feedstocks showed a notable enhancement, implying that the interaction between the two feedstocks promoted the generation of organics with larger π-conjugated structures. With regard to SM1CM1, the intensity of region IV was the highest, which was consistent with the 2D fluorescence results. Besides, the intensity of region V from the combined feedstocks was lower than that of the single feedstock. This phenomenon implied that the co-HTC of the feedstock mixtures would impact the reaction processes such as hydrolysis, condensation, and re-polymerization, which further affected the polymeric structure of the hydrochar.

3.7. Co-HTC mechanism

Based on the experimental results, the possible co-HTC mechanisms of SM and CM are proposed in Fig. S3 in the Supplementary Material. Animal manure mainly consists of carbohydrates, proteins, and lipids, which degrade into different fragments

during the reaction process (Lv et al., 2010; Provenzano et al., 2014). During HTC, the carbohydrate fractions were hydrolyzed into sugar derivatives at low temperatures. The produced monosaccharides such as fructose and glucose were then transformed into furan derivatives, which could form carbonaceous materials through polymerization and aggregation reactions. Furthermore, the monosaccharides could also be converted into cyclopentenone derivatives, which were the major ketone compounds in the liquid product. Meanwhile, the amino acids derived from protein conversion could either degrade into carboxylic acids and amines or condense with carbonyl to form pyrrole species (He et al., 2013). The mutual interaction between the amino acids and sugars generated nitrogenous compounds through the Maillard reaction, which could further transform into a solid residue via polymerization. In addition, under HTC conditions, the lipid fractions were readily decomposed into fatty acids and glycerin by hydrolysis. Subsequently, the glycerol was transformed into a range of aldehydes, ketones, and alcohols via a series of degradation pathways, and the formed alcohol species could react with fatty acids to produce esters (Pedersen et al., 2015). Additionally, with sufficient carbonization time, certain reactive intermediates produced from the degradation of manure components could mutually interact to form large substances, which were further converted into solid particles through re-polymerization, condensation, and aromatization. Simultaneously, some chemical species were also transformed into the aqueous phase.

4. Conclusions

This study investigated the co-HTC of SM and CM with various mixing ratios, and analyzed the properties of the derived hydrochar and liquid. The results demonstrated that the mutual interaction of the reaction intermediates from different types of animal manure promoted the formation of hydrochar. Additionally, the synergistic effects during the co-HTC were beneficial to N and C enrichment in the hydrochar owning to the enhanced re-polymerization and carbonization. The co-HTC of the manure mixture also boosted the deoxygenation and as a result improved the fuel

properties of the hydrochar compared with the HTC of individual feedstock. This was confirmed by the lower O/C ratio and higher energy yield. The combustibility of the co-HTC hydrochar was upgraded with respect to the ignition temperature and comprehensive combustion index. Furthermore, the co-HTC interactions in the mixed feedstocks favored the formation of organic acids and polymeric species with π-conjugated structures, and influenced the transfer of nitrogenous species in the liquid products. This study demonstrated that co-HTC of SM and CM was advantageous in producing hydrochar with improved properties than those from the individual treatment.

Acknowledgements

This work was supported by the Natural Science Fund of Shandong Province (ZR2019BB051), the National Natural Science Foundation of China (No. 51876080), the Program for Taishan Scholars of Shandong Province Government, the Recruitment Program of Global Young Experts (Thousand Youth Talents Plan), the Natural Science Fund of Shandong Province (ZR2017BB002), the Key R&D Program of Shandong Province (2018GSF116014), and a Korea University Grant.

References

Apaydın-Varol, E., Pütün, A.E. 2012. Preparation and characterization of pyrolytic chars from different biomass samples. J. Anal. Appl Pyrol., 98, 29-36.

Cantero-Tubilla, B., Cantero, D.A., Martinez, C.M., Tester, J.W., Walker, L.P., Posmanik, R. 2018. Characterization of the solid products from hydrothermal liquefaction of waste feedstocks from food and agricultural industries. J. Supercrit. Fluid. 133, 665-673.

Cao, X., Harris, W. 2010. Properties of dairy-manure-derived biochar pertinent to its potential use in remediation. Bioresour. Technol., 101, 5222-5228.

Cao, X., Ro, K.S., Chappell, M., Li, Y., Mao, J. 2011. Chemical structures of swine-manure chars produced under different carbonization conditions investigated by advanced solid-state ^{13}C nuclear magnetic resonance (NMR) spectroscopy. Energy Fuels 25, 388-397.

Channiwala, S., Parikh, P. 2002. A unified correlation for estimating HHV of solid, liquid and gaseous fuels. Fuel 81, 1051-1063.

Chen, W., Chen, Y.Q., Yang, H.P., Xia, M.W., Li, K.X., Chen, X., Chen, H.P. 2017. Co-pyrolysis of lignocellulosic biomass and microalgae: Products characteristics and interaction effect. Bioresour. Technol., 245, 860-868.

Chen, W., Westerhoff, P., Leenheer, J.A., Booksh, K. 2003. Fluorescence excitation−emission matrix regional integration to quantify spectra for dissolved organic matter. Environ Sci. Technol. 37, 5701-5710.

Chen, X., Ma, X., Peng, X., Lin, Y., Yao, Z. 2018. Conversion of sweet potato waste to solid fuel via hydrothermal carbonization. Bioresour. Technol. 249, 900-907.

de Oliveira Silva, J., Rodrigues Filho, G., da Silva Meireles, C., Ribeiro, S.D., Vieira, J.G., da Silva, C.V., Cerqueira, D.A. 2012. Thermal analysis and FTIR studies of sewage sludge produced in treatment plants. The case of sludge in the city of Uberlândia-MG, Brazil. Thermochimica Acta 528, 72-75.

Deng, W., Zhang, Q., Wang, Y. 2014. Catalytic transformations of cellulose and cellulose-derived carbohydrates into organic acids. Catal. Today 234, 31-41.

Funke, A., Ziegler, F. 2010. Hydrothermal carbonization of biomass: a summary and discussion of chemical mechanisms for process engineering. Biofuel Bioprod. Biorefin. 4, 160-177.

Guo, X., Gu, J., Gao, H., Qin, Q., Chen, Z., Shao, L., Chen, L., Li, H., Zhang, W., Chen, S. 2012. Effects of Cu on metabolisms and enzyme activities of microbial communities in the process of composting. Bioresour. Technol. 108, 140-148.

He, C., Giannis, A., Wang, J.Y. 2013. Conversion of sewage sludge to clean solid fuel using hydrothermal carbonization: hydrochar fuel characteristics and combustion behavior. Appl. Energ. 111, 257-266.

Heidari, M., Norouzi, O., Salaudeen, S., Acharya, B., Dutta, A. 2019. Prediction of hydrothermal carbonization with respect to the biomass components and severity factor. Energy Fuels 33, 9916-9924.

Hu, Y., Cheng, H., Tao, S. 2017. Environmental and human health challenges of industrial livestock and poultry farming in China and their mitigation. Environ. Int. 107, 111-130.

Kang, J., Duan, X., Wang, C., Sun, H., Tan, X., Tade, M.O., Wang, S. 2018. Nitrogen-doped bamboo-like carbon nanotubes with Ni encapsulation for persulfate activation to remove emerging contaminants with excellent catalytic stability. Chem. Eng. J. 332, 398-408.

Kim, D., Lee, K., Park, K.Y. 2014. Hydrothermal carbonization of anaerobically digested sludge for solid fuel production and energy recovery. Fuel 130, 120-125.

Kim, D., Lee, K., Park, K.Y. 2016. Upgrading the characteristics of biochar from cellulose, lignin, and xylan for solid biofuel production from biomass by hydrothermal carbonization. J. Ind. Eng. Chem. 42, 95-100.

Lang, Q., Chen, M., Guo, Y., Liu, Z., Gai, C. 2019a. Effect of hydrothermal carbonization on heavy metals in swine manure: speciation, bioavailability and environmental risk. J. Environ. Manage. 234, 97-103.

Lang, Q., Guo, Y., Zheng, Q., Liu, Z., Gai, C. 2018. Co-hydrothermal carbonization of lignocellulosic biomass and swine manure: Hydrochar properties and heavy metal

transformation behavior. Bioresour. Technol. 266, 242-248.

Lang, Q., Zhang, B., Liu, Z., Jiao, W., Xia, Y., Chen, Z., Li, D., Ma, J., Gai, C. 2019b. Properties of hydrochars derived from swine manure by CaO assisted hydrothermal carbonization. J. Environ. Manage. 233, 440-446.

Li, H., Liu, Z., Zhang, Y., Li, B., Lu, H., Duan, N., Liu, M., Zhu, Z., Si, B. 2014. Conversion efficiency and oil quality of low-lipid high-protein and high-lipid low-protein microalgae via hydrothermal liquefaction. Bioresour. Technol. 154, 322-329.

Li, Y., Liu, H., Xiao, K., Jin, M., Xiao, H., Yao, H. 2019a. Combustion and Pyrolysis Characteristics of Hydrochar Prepared by Hydrothermal Carbonization of Typical Food Waste: Influence of Carbohydrates, Proteins, and Lipids. Energy Fuels 34, 430-439.

Li, Y., Liu, H., Xiao, K., Liu, X., Hu, H., Li, X., Yao, H. 2019b. Correlations between the physicochemical properties of hydrochar and specific components of waste lettuce: Influence of moisture, carbohydrates, proteins and lipids. Bioresour. Technol. 272, 482-488.

Lievens, C., Mourant, D., He, M., Gunawan, R., Li, X., Li, C.Z. 2011. An FT-IR spectroscopic study of carbonyl functionalities in bio-oils. Fuel 90, 3417-3423.

Liu, H., Chen, Y., Yang, H., Gentili, F.G., Söderlind, U., Wang, X., Zhang, W., Chen, H. 2019. Hydrothermal carbonization of natural microalgae containing a high ash content. Fuel 249, 441-448.

Lu, X., Berge, N.D. 2014. Influence of feedstock chemical composition on product formation and characteristics derived from the hydrothermal carbonization of mixed feedstocks. Bioresour. Technol. 166, 120-131.

Luo, G.E., Strong, P.J., Wang, H., Ni, W., Shi, W. 2011. Kinetics of the pyrolytic and hydrothermal decomposition of water hyacinth. Bioresour. Technol. 102, 6990-6994.

Lv, D., Xu, M., Liu, X., Zhan, Z., Li, Z., Yao, H. 2010. Effect of cellulose, lignin, alkali and alkaline earth metallic species on biomass pyrolysis and gasification. Fuel

Process. Technol. 91, 903-909.

Mau, V., Quance, J., Posmanik, R., Gross, A. 2016. Phases' characteristics of poultry litter hydrothermal carbonization under a range of process parameters. Bioresour. Technol. 219, 632-642.

He, M.M., Li, W.H., Liang, X.Q., Wu, D.L., Tian, G.M. 2009. Effect of composting process on phytotoxicity and speciation of copper, zinc and lead in sewage sludge and swine manure. Waste Manage. 29, 590-597.

Mourant, D., Lievens, C., Gunawan, R., Wang, Y., Hu, X., Wu, L.P., Syed-Hassan, S.S.A., Li, C.Z. Effects of temperature on the yields and properties of bio-oil from the fast pyrolysis of mallee bark. Fuel 108, 400-408.

Nogueira, G.D., Duarte, C.R., Barrozo, M.A. 2019. Hydrothermal carbonization of acerola (Malphigia emarginata DC) wastes and its application as an adsorbent. Waste Manage. 95, 466-475.

Parshetti, G.K., Hoekman, S.K., Balasubramanian, R. 2013. Chemical, structural and combustion characteristics of carbonaceous products obtained by hydrothermal carbonization of palm empty fruit bunches. Bioresour. Technol. 135, 683-689.

Pedersen, T.H., Jasiūnas, L., Casamassima, L., Singh, S., Jensen, T., Rosendahl, L.A. 2015. Synergetic hydrothermal co-liquefaction of crude glycerol and aspen wood. Energy Convers. Manag. 106, 886-891.

Peng, C., Zhai, Y., Zhu, Y., Xu, B., Wang, T., Li, C., Zeng, G. 2016. Production of char from sewage sludge employing hydrothermal carbonization: char properties, combustion behavior and thermal characteristics. Fuel 176, 110-118.

Provenzano, M.R., Malerba, A.D., Pezzolla, D., Gigliotti, G. 2014. Chemical and spectroscopic characterization of organic matter during the anaerobic digestion and successive composting of pig slurry. Waste Manage. 34, 653-660.

Sharma, H.B., Sarmah, A.K., Dubey, B. 2020. Hydrothermal carbonization of renewable waste biomass for solid biofuel production: A discussion on process mechanism, the influence of process parameters, environmental performance and fuel properties of hydrochar. Renew. Sust. Energ. Rev. 123, 109761.

Singh, R., Prakash, A., Dhiman, S.K., Balagurumurthy, B., Arora, A.K., Puri, S., Bhaskar, T. 2014. Hydrothermal conversion of lignin to substituted phenols and aromatic ethers. Bioresour. Technol. 165, 319-322.

Tan, X.F., Liu, Y.G., Gu, Y.L., Xu, Y., Zeng, G.-m., Hu, X.J., Liu, S.B., Wang, X., Liu, S.M., Li, J. 2016. Biochar-based nano-composites for the decontamination of wastewater: a review. Bioresour. Technol. 212, 318-333.

Tymchyshyn, M., Xu, C.C. 2010. Liquefaction of bio-mass in hot-compressed water for the production of phenolic compounds. Bioresour. Technol. 101, 2483-2490.

Wang, L., Chang, Y., Liu, Q. 2019. Fate and distribution of nutrients and heavy metals during hydrothermal carbonization of sewage sludge with implication to land application. J. Clean. Prod. 225, 972-983.

Wang, T., Zhai, Y., Zhu, Y., Li, C., Zeng, G. 2018a. A review of the hydrothermal carbonization of biomass waste for hydrochar formation: Process conditions, fundamentals, and physicochemical properties. Renew. Sust. Energ. Rev. 90, 223-247.

Wang, T., Zhai, Y., Zhu, Y., Peng, C., Xu, B., Wang, T., Li, C., Zeng, G. 2018b. Influence of temperature on nitrogen fate during hydrothermal carbonization of food waste. Bioresour. Technol. 247, 182-189.

Wei, X., Ma, X., Peng, X., Yao, Z., Yang, F., Dai, M. 2018. Comparative investigation between co-pyrolysis characteristics of protein and carbohydrate by TG-FTIR and Py-GC/MS. J. Anal. Appl Pyrol. 135, 209-218.

Wilson, C.A., Novak, J.T. 2009. Hydrolysis of macromolecular components of primary and secondary wastewater sludge by thermal hydrolytic pretreatment. Water Res. 43, 4489-4498.

Xin, Y., Wang, D., Li, X.Q., Yuan, Q., Cao, H. 2018. Influence of moisture content on cattle manure char properties and its potential for hydrogen rich gas production. J. Anal. Appl Pyrol. 130, 224-232.

Xu, Z.X., Song, H., Deng, X.Q., Zhang, Y.Y., Ma, X.Q., M., Tong, S.Q., He, Z.X., Wang, Q., Shao, Y.W., Hu, X. 2019a. Dewatering of sewage sludge via thermal hydrolysis

with ammonia-treated Fenton iron sludge as skeleton material. J. Hazard. Mater. 379, 120810.

Xu, Z.X., Song, H., Li, P.J., He, Z.X., Wang, Q., Wang, K., Duan, P.G. 2020. Hydrothermal carbonization of sewage sludge: Effect of aqueous phase recycling. Chem. Eng. J. 387, 123410.

Xu, Z.X., Song, H., Zhang, S., Tong, S.Q., He, Z.X., Wang, Q., Li, B., Hu, X. 2019b. Co-hydrothermal carbonization of digested sewage sludge and cow dung biogas residue: Investigation of the reaction characteristics. Energy 187, 115972.

Xu, Z.X., Xu, L., Cheng, J.H., He, Z.X., Wang, Q., Hu, X. 2018. Investigation of pathways for transformation of N-heterocycle compounds during sewage sludge pyrolysis process. Fuel Process. Technol. 182, 37-44.

Yuan, T., Cheng, Y., Huang, W., Zhang, Z., Lei, Z., Shimizu, K., Utsumi, M. 2018. Fertilizer potential of liquid product from hydrothermal treatment of swine manure. Waste manage. 77, 166-171.

Zhai, Y., Pang, D., Chen, H., Xiang, B., Chen, J., Li, C., Zeng, G., Qiu, L. 2013. Effects of ammonization on the surface physico-chemical properties of sludge-based activated carbon. Appl. Surf. Sci. 280, 590-597.

Zhang, L., Wang, Q., Wang, B., Yang, G., Lucia, L.A., Chen, J. 2015. Hydrothermal carbonization of corncob residues for hydrochar production. Energy Fuels 29, 872-876.

Zheng, C., Ma, X., Yao, Z., Chen, X. 2019. The properties and combustion behaviors of hydrochars derived from co-hydrothermal carbonization of sewage sludge and food waste. Bioresour. Technol. 285, 121347.

Zhou, Y., Engler, N., Li, Y., Nelles, M. 2020. The influence of hydrothermal operation on the surface properties of kitchen waste-derived hydrochar: Biogas upgrading. J. Clean. Prod. 121020.

Figures

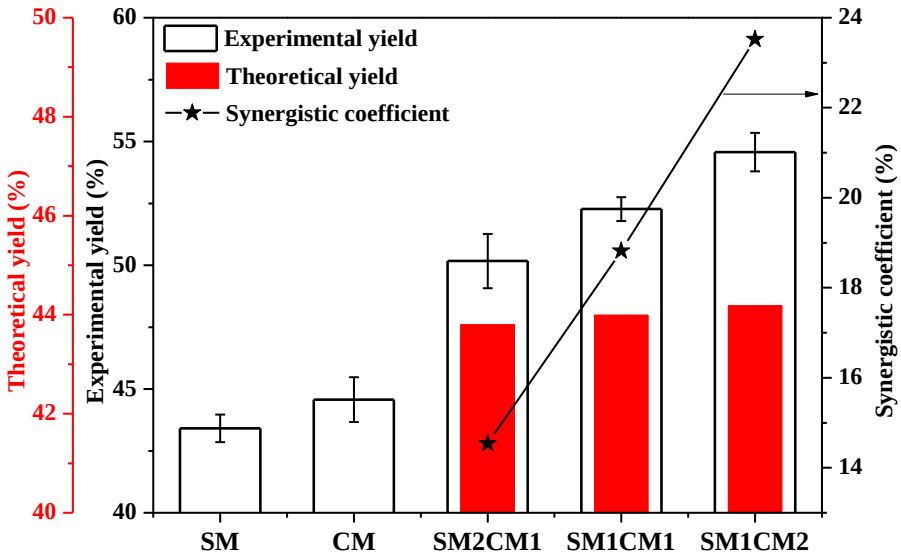

Fig. 1. The yield of solid products from the HTC of the single feedstocks and the manure mixtures with varied mass ratios. The experimental conditions for the HTC were 240 ºC and 10 h.

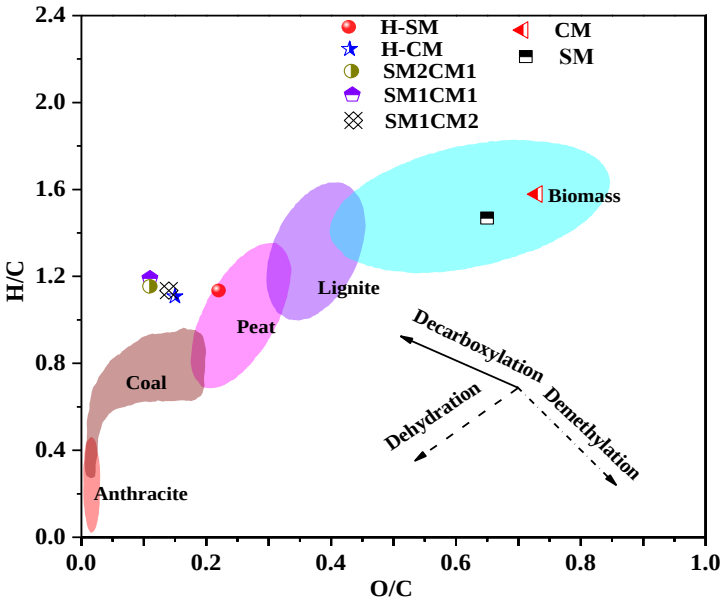

Fig. 2. Van Krevelen diagram for the feedstocks and hydrochars derived from different reaction systems.

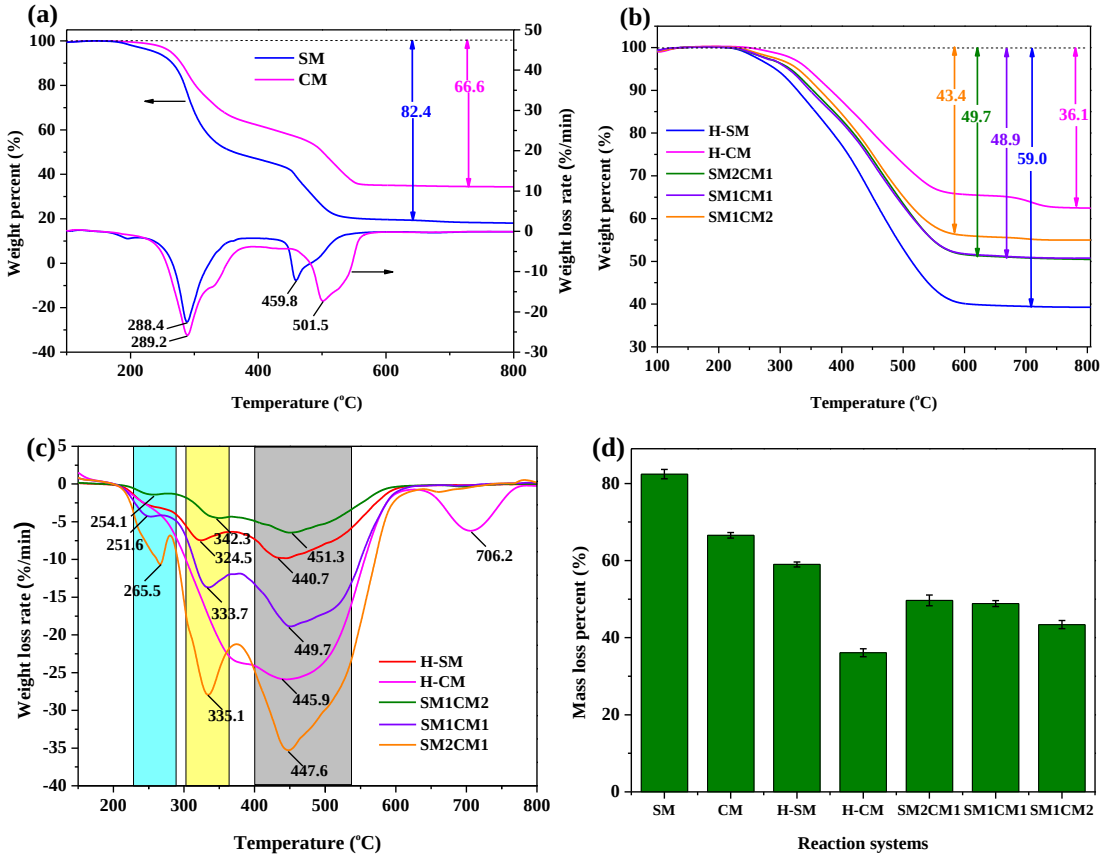

Fig. 3. TG-DTG profiles of the feedstocks (a) and the derived hydrochars (b and c); the mass loss percentage from all solid samples (d).

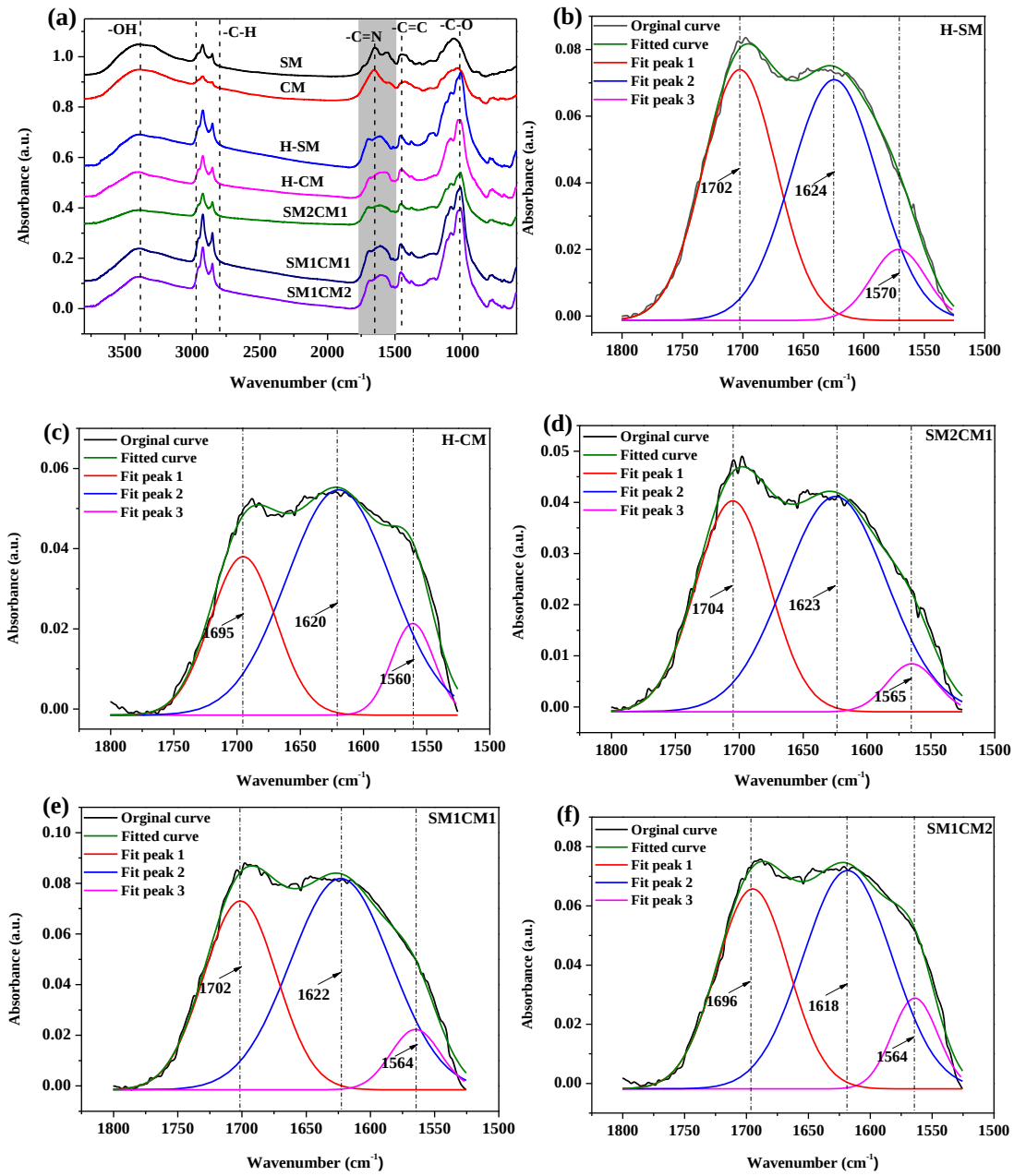

Fig. 4. FTIR spectra of the feedstocks and derived hydrochars (a); the spectral deconvolution at the 1850-1500 cm^{-1} band region of the hydrochars: H-SM (b), H-CM (c), SM2CM1 (d), SM1CM1 (e), and SM1CM2 (f).

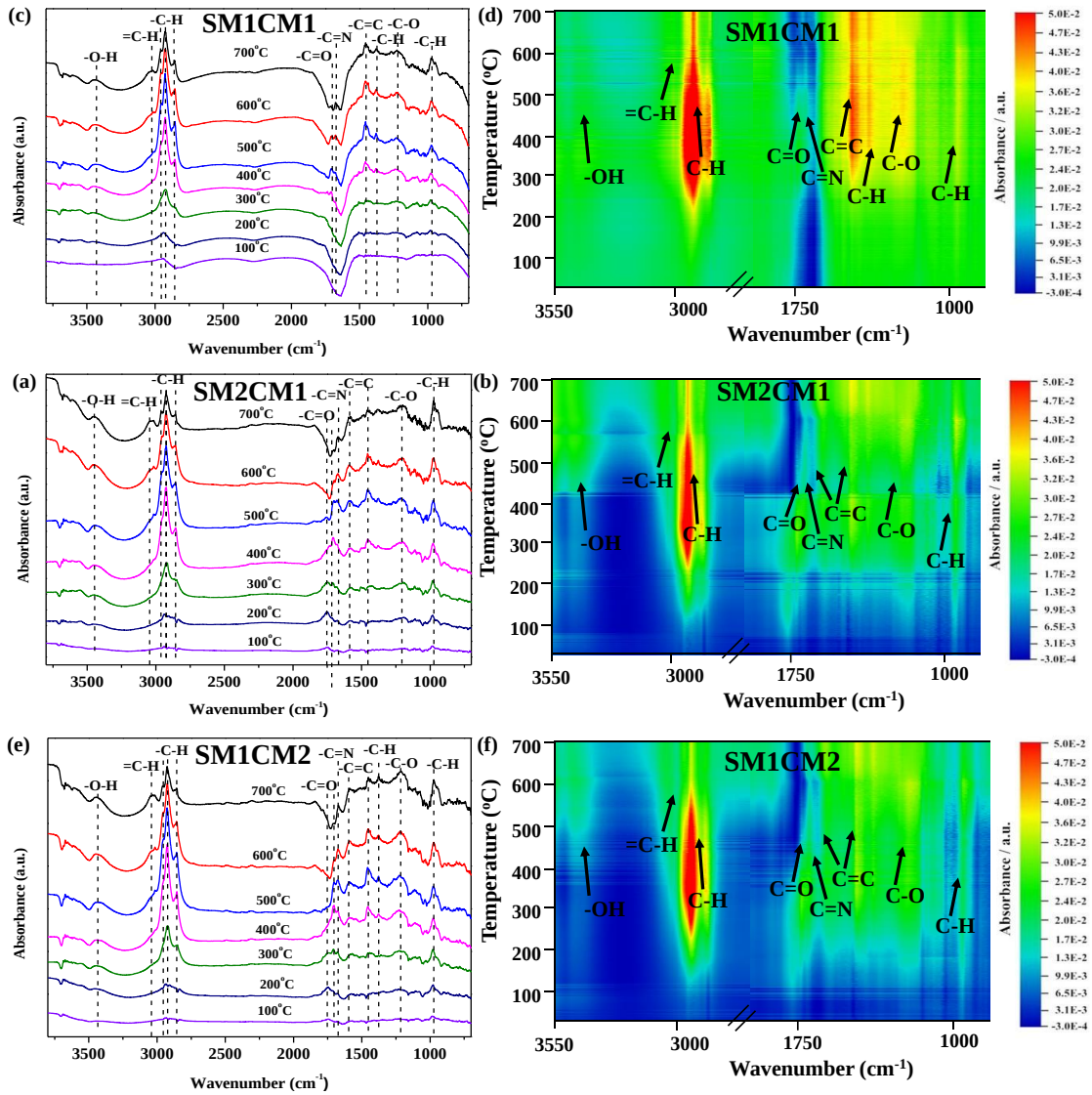

Fig. 5. DRIFTS results of the derived hydrochar: SM2CM1 (a), SM1CM1 (c), and SM1CM2 (e); (b), (d), and (f) are the corresponding 2D DRIFT spectra.

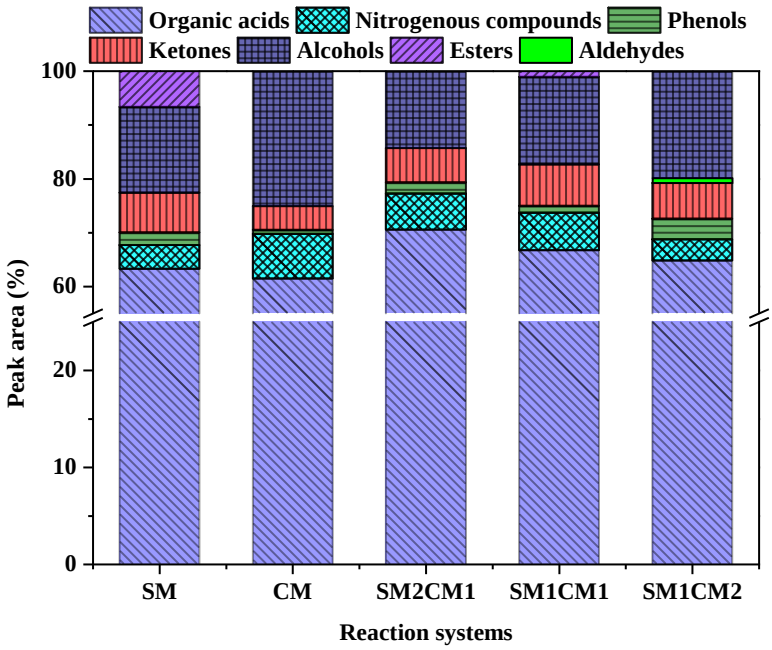

Fig. 6. GC-MS analysis of the liquid components derived from different systems.

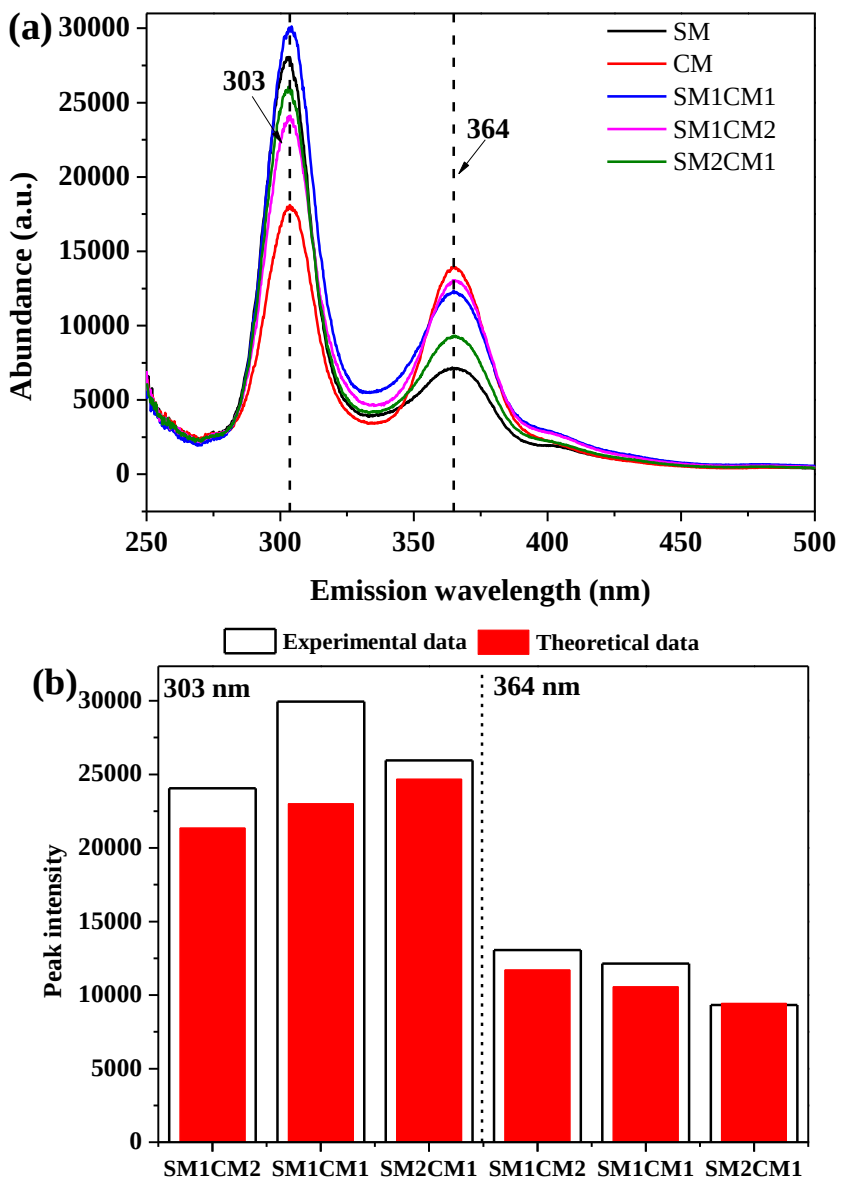

Fig. 7. UV-fluorescence spectra of the derived liquid products (a), and the difference between the experimental and theoretical peak intensity at 303 and 364 nm (b).

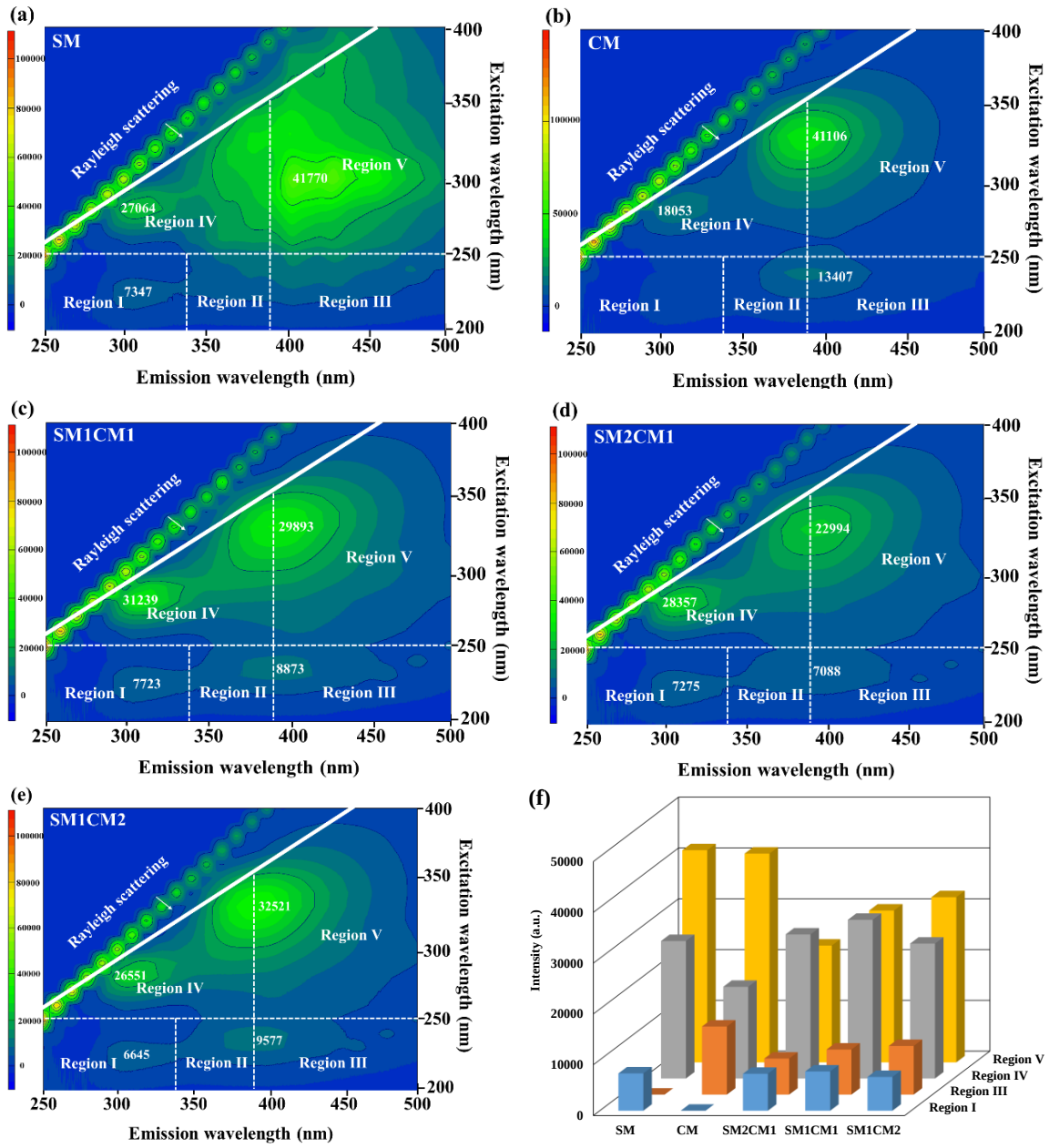

Fig. 8. 3D UV-fluorescence spectra for the liquid fraction derived from different reaction conditions.

Tables

Table 1. Ultimate analysis, atomic ratio, and recovery rate of solid samples (wt.%, dry basis).

Sample	Ultimate analysis (db, %)					Atomic ratio		Recovery rate (%)	
	C	H	N	O[a]	S	H/C	O/C	C recovery rate	N recovery rate
SM	37.19±0.70	4.93±0.18	2.14±0.11	32.27±0.03	0.25±0.02	1.59±0.02	0.65±0.01	-	-
CM	30.4±0.80	4.32±0.25	3.22±0.14	29.66±0.30	0.35±0.14	1.71±0.14	0.73±0.01	-	-
H-SM	40.61±0.91	4.15±0.10	2.11±0.12	11.72±1.29	0.18±0.03	1.23±0.00	0.22±0.03	47.40±0.75	42.79±0.29
H-CM	28.44±1.08	2.84±0.13	2.05±0.17	5.65±0.05	0.25±0.01	1.20±0.10	0.15±0.01	41.69±1.08	28.33±0.72
SM2CM1	39.74±0.29	4.15±0.12	2.26±0.12	5.58±1.10	0.17±0.02	1.25±0.03	0.11±0.02	57.08±0.25	45.36±2.62
SM1CM1	38.19±0.17	4.11±0.10	2.42±0.09	5.38±1.69	0.20±0.02	1.29±0.03	0.11±0.03	59.07±1.15	47.21±2.13
SM1CM2	34.54±0.76	3.80±0.08	2.17±0.01	5.39±0.40	0.20±0.05	1.32±0.03	0.12±0.01	57.69±0.10	41.41±0.03

[a] Calculated by difference: O%=100%-C%-H%-N%-S%-ash% (dry basis)

Table 2. Proximate analysis, HHV, and energy yield of the solid samples.

Sample	Proximate analysis (%)				HHV (MJ/Kg)	Energy yield (%)
	Moisture	Fixed carbon[a]	Volatile matter	Ash		
SM	8.32±0.08	17.86±1.46	50.60±0.60	23.22±0.78	14.96±0.47	-
CM	7.63±0.17	15.25±1.75	45.07±1.07	32.05±0.85	11.95±0.01	-
H-SM	0.93±0.05	20.31±0.59	37.53±0.11	41.23±0.43	16.97±0.56	49.25±0.68
H-CM	0.61±0.07	14.53±1.00	24.09±0.21	60.77±0.72	11.40±0.25	42.55±1.56
SM2CM1	0.76±0.08	21.19±1.00	29.95±0.53	48.10±0.55	17.15±0.34	61.68±0.52
SM1CM1	0.41±0.04	19.26±0.93	30.63±0.42	49.70±1.31	16.55±0.32	64.32±0.98
SM1CM2	0.89±0.07	17.28±0.62	27.93±0.33	53.90±0.22	14.83±0.21	62.48±0.78

[a] Calculated by difference: Fixed carbon%=100%-moisture%-volatile matter%-ash%

Table 3. Synergistic coefficient of various parameters from the hydrochars.

Synergistic coefficient (%)	Samples		
	SM2CM1	SM1CM1	SM1CM2
C content	8.72±0.06	10.62±0.76	6.28±0.98
Fixed carbon	15.24±0.88	10.55±0.29	5.06±1.75
C recovery rate	25.46±0.94	32.59±0.53	32.35±1.64
Energy yield	31.18±0.93	40.12±0.31	39.53±0.79

Table 4. Combustion parameters of the feedstocks and derived hydrochars.

Sample	T_i[a] (ºC)	T_f[b] (ºC)	T_{p1}[c] (ºC)	DTG_1[d] (%/min)	T_{P2}[c] (ºC)	DTG_2[d] (%/min)	T_{P3}[c] (ºC)	DTG_3[d] (%/min)	S (10^{-6} ºC $^{-3}$ min^{-2})
SM	260.4	510.5	-		288.4	-22.2	459.8	-12.3	3.4
CM	262.5	555.3	-		289.2	-25.7	501.5	-17.3	2.7
H-SM	264.8	552.2	-		324.5	-7.7	440.7	-9.9	0.97
H-CM	318.4	743.4	-		445.9	-26.0	706.2	-6.2	0.57
SM2CM1	229.3	553.9	265.5	-10.6	335.1	-28.1	447.6	-35.3	3.4
SM1CM1	220.2	560.8	251.6	-4.3	333.7	-13.7	449.7	-19.0	1.9
SM1CM2	222.7	543.2	254.1	-1.5	342.3	-4.5	451.3	-6.5	0.61

[a] T_i: the ignition temperature (ºC).

[b] T_f: the burnout temperature (ºC).

[c] T_{p1}, T_{p2}, T_{p3}: peak temperature (ºC).

[d] DTG_1, DTG_2, DTG_3: corresponding mass loss rate.

Table 5. Kinetic parameters of the feedstocks and derived hydrochars.

Sample	Stage 1			Stage 2			Stage 3		
	T_r[a]	E[b]	R^2[c]	T_r	E	R^2	T_r	E	R^2
SM	-	-	-	230-350	57.0	0.990	420-540	54.4	0.997
CM	-	-	-	220-380	59.0	0.996	440-590	26.2	0.957
H-SM	-	-	-	270-360	36.0	0.998	380-600	37.1	0.999
H-CM	-	-	-	230-600	36.6	0.999	630-770	58.6	0.934
SM2CM1	200-280	66.7	0.992	285-370	49.0	0.995	380-610	40.3	0.999
SM1CM1	210-270	41.9	0.998	280-370	41.8	0.998	385-620	39.3	0.999
SM1CM2	210-280	28.6	0.996	285-370	44.2	0.996	380-600	43.7	0.999

[a] T_r: temperature range (°C).

[b] E: activation energy (KJ/mol).

[c] R^2: correlation coefficient.

Supplementary material

Co-hydrothermal carbonization of swine and chicken manure: Influence of cross-interaction on hydrochar and liquid characteristics

Qingyin Li[a], Shu Zhang[b], Mortaza Gholizadeh[c], Xun Hu[a,*], Xiangzhou Yuan[d,e **], Binoy Sarkar[f], Meththika Vithanage[g], Ondřej Mašek[h], Yong Sik Ok[e, ***]

[a] School of Materials Science and Engineering, University of Jinan, Jinan 250022, P. R. China

[b] College of Material Science and Engineering, Nanjing Forestry University, Nanjing, 210037, Jiangsu, China

[c] Faculty of Chemical and Petroleum Engineering, University of Tabriz, Tabriz, Iran

[d] Department of Chemical & Biological Engineering, Korea University, 145 Anam-ro, Seongbuk-gu, Seoul 02841, Republic of Korea

[e] Korea Biochar Research Center & APRU Sustainable Waste Management Program, & Division of Environmental Science and Ecological Engineering, Korea University, Seoul 02841, Republic of Korea

[f] Lancaster Environment Centre, Lancaster University, Lancaster, LA1 4YQ, United Kingdom

[g] Ecosphere Resilience Research Center, Faculty of Applied Sciences, University of Sri Jayewardenepura, Nugegoda 10250, Sri Lanka

[h] UK Biochar Research Centre, School of Geosciences, University of Edinburgh Alexander Crum Brown Road, Crew Building-EH9 3JN, Edinburgh, UK

* Corresponding author: E-mail address: Xun.Hu@outlook.com

** Corresponding author: E-mail address: yuan0125@korea.ac.kr

*** Corresponding author: E-mail: yongsikok@korea.ac.kr

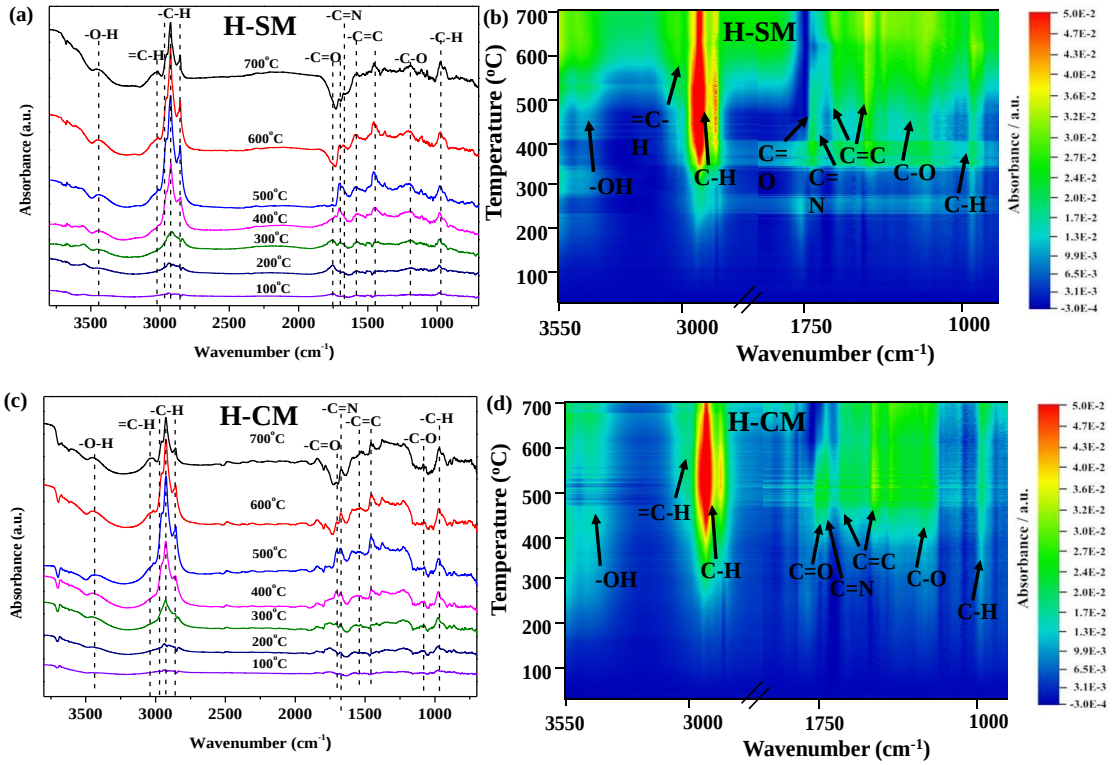

Fig. S1. DRIFTS results of the derived hydrochar: H-SM (a) and H-CM (c); (b) and (d) are the corresponding 2D-DRIFT spectra.

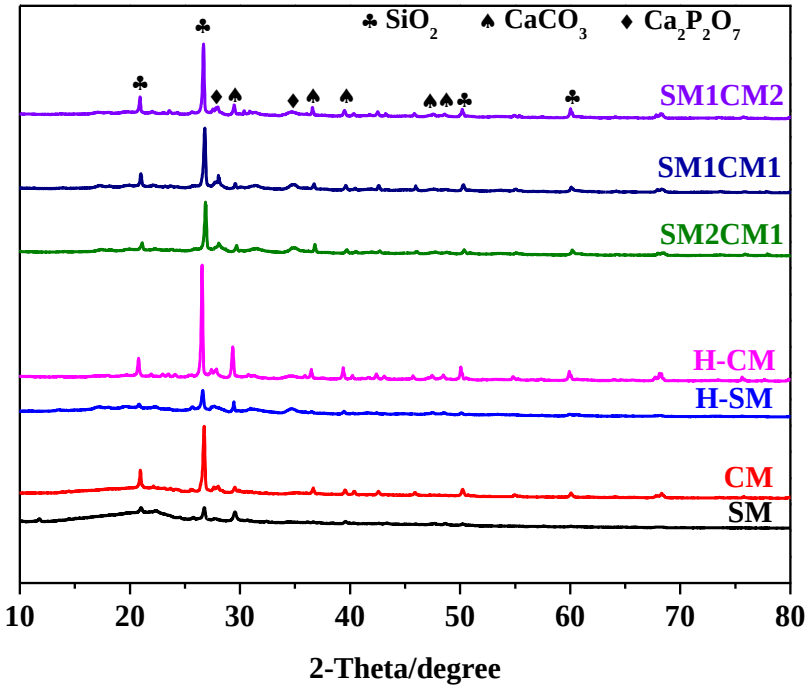

Fig. S2. XRD patterns of the feedstocks and derived hydrochars.

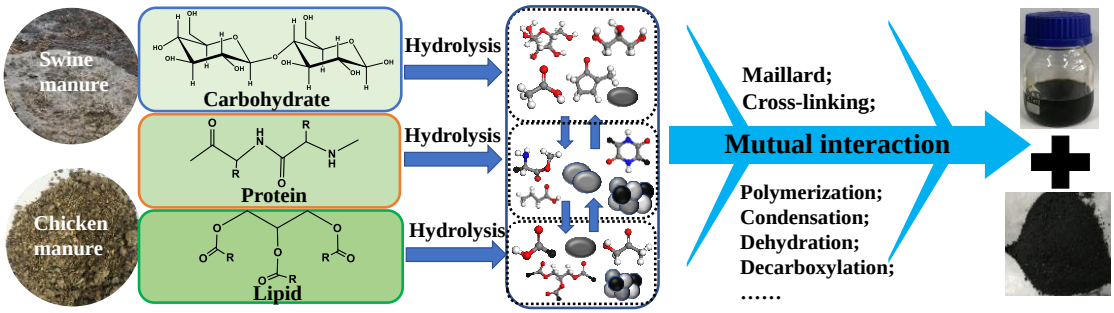

Fig. S3. Co-HTC mechanism of SM and CM.

Table S1. Crystalline sizes of key mineral phases in the feedstocks and hydrochars obtained in different reaction systems.

Solid sample	Crystalline sizes (nm)		
	SiO_2	$CaCO_3$	$Ca_2P_2O_7$
SM	33.1	22.2	25.6
CM	39.8	23.0	35.3
H-SM	36.7	14.2	56.4
H-CM	49.8	40.8	26.2
SM2CM1	40.8	19.8	48.4
SM1CM1	40.2	27.0	45.9
SM2CM1	47.5	26.2	41.4

Table S2. Compositional analysis of the liquid product derived from the HTC of the individual feedstocks and their mixtures.

Compound	Relative content (%)				
	SM	CM	SM2CM1	SM1CM1	SM1CM2
Organic acids					
Acetic acid	33.36	61.48	41.61	39.36	45.49
Propanoic acid	13.72	-	13.58	12.13	9.17
Butanoic acid	12.43	-	12.57	12.37	2.08
Hexanoic acid	2.54	-	2.80	2.87	8.08
Propanedioic acid, propy-	1.24	-	-	-	-
Ketones					
2-Piperidinone	5.70	-	4.47	3.86	3.02
2(1H)-Pyridone, 6-methyl-	-	-	0.97	-	1.57
4,4-Dimethyl-2-cyclopenten-1-one	-	-	0.44	-	-
(S)-(+)-2',3'-Dideoxyribonolactone	-	-	0.49	-	-
2-Pyrrolidinone	1.66	4.43	-	2.84	2.05
2,5-Pyrrolidinedione, 1-methyl-	-	-	-	1.03	-
Nitrogenous compound					
Acetamide	2.20	-	3.81	-	1.99
Propanediamide	1.80		-	4.42	-
Propanamide	0.40		-	1.27	-
Butanamide	-	-	-	1.28	0.79
Urazole	-	-	-	-	1.16
Formamide, N, N-dimethyl-	-	-	1.13	-	-
Pentanamide, 5-hydroxy-	-	-	1.42		-
Pyrazine, 5-butyl-2,3-dimethyl-	-	-	0.33		-

2-Amino-4-methylpyrimidine	-	2.84	-		-
3,5-Dimethyl-1-butylpyrazole	-	4.04	-		-
Pyrrole, 2,3,4,5-tetramethyl-	-	1.41	-		-
Phenols					
Mequinol	1.17	-	1.13	-	0.92
Phenol, 3-methyl-	0.48	0.74	-	-	-
3-Pyridinol	0.71	-	-	-	-
Phenol	-	-	0.95	0.68	0.91
Phenol, 4-methoxy-	-	-	-	0.59	1.97
Alcohols					
3-Pyridinol	15.95	25.07	13.34	14.07	19.89
3-Pyridinol, 6-methyl-	-	-	0.95	1.07	-
3-Pyridinol, 2-methyl-	-	-	-	1.11	-
Esters					
Diethyl Phthalate	6.29	-	-	-	-
Pyridin-3-yl 2-methylbutanoate	0.36	-	-	-	-
2-Hydroxy-gamma-butyrolactone	-	-	-	1.04	-
Aldehydes					
Butanal, O-methyloxime	-	-	-	-	0.91